RESEARCH PAPER

Test Methods for the Mechanical Characterization of Flexure Hinges

P. Meyer[1] · J. Finder[1,2] · C. Hühne[1,3]

Abstract

Background The design of compliant mechanisms requires detailed knowledge about the stiffness properties of their flexible segments. However, there are no standardized test methods for flexure hinges, and therefore the influence of manufacturing-specific effects, such as anisotropy, on the stiffness properties cannot be quantified.

Objective This paper presents novel test methods for variable cross-section flexure hinges subjected to large deformations and pure bending loading, which determine the bending stiffness of flexure hinges over their entire deflection range using a universal testing machine.

Methods The novel test methods for flexure hinges are based on the tensile test, the four-point bending test (FPBT), and the column bending test (CBT). These test methods were initially formulated for constant cross-section specimens, but are adapted in this study to examine variable cross-section specimens. The derived test methods are validated by using isotropic materials with well-known properties and by comparing the calculated deflections with deflections measured by means of image processing.

Results The deflection validation shows that the adapted CBT (aCBT) is accurate over the entire deflection range, achieving curvature of up to $\kappa = 0.40$ mm^{-1}, whereas the maximum curvature in the adapted FPBT (aFPBT) is limited by the test methodology to about $\kappa = 0.15$ mm^{-1}. At small strains, the flexural modulus determined in the aCBT and aFPBT agrees well with the Young's modulus determined in the tensile test, as would be expected for isotropic materials.

Conclusion The aCBT proves to be a suitable test method for flexure hinges at large deflections, whereas the stiffness characterization at small deflections can be performed with both the aCBT and the aFPBT. The presented test methods validated on isotropic materials form the basis for characterizing anisotropic flexure hinges with geometry-dependent stiffness properties.

Keywords Compliant mechanism · Pseudo-rigid-body model · Four-point bending · Column bending test · Machine compliance · Gauge length

Introduction

Compliant mechanisms offer great advantages compared to conventional rigid-body mechanisms. The advantages include reduced part count, increased precision and reliability, predictable backlash-free motion, reduced maintenance and wear, and lightweight designs. However, compliant mechanisms are much more difficult to design than conventional mechanisms because the movement results from a deformation of the structure.

A simple method to design and analyze compliant mechanisms subjected to large deflections are pseudo-rigid-body models (PRBM) [1]. PRBM predict the deflection path and the force–deflection relationship of flexible segments by replacing them with rigid links connected by discrete pin joints. One way to allow motion in compliant mechanisms is through small-length flexural pivots (SLFP), which describe

✉ P. Meyer
pat.meyer@tu-braunschweig.de

J. Finder
j.finder@tu-braunschweig.de

C. Hühne
christian.huehne@dlr.de

1   Institute of Mechanics and Adaptronics, Technische Universität Braunschweig, Langer Kamp 6, 38106 Braunschweig, Germany

2   Institute of Aircraft Design and Lightweight Structures, Technische Universität Braunschweig, Hermann-Blenk-Straße 35, 38108 Braunschweig, Germany

3   Institute of Lightweight Systems, German Aerospace Center, Lilienthalplatz 7, 38108 Braunschweig, Germany

flexible segments small in lengths and bending stiffness compared to the segments to which they are attached [2]. As shown in Fig. 1, the SLFP is modeled by torsion springs attached to the pin joints with the equivalent stiffness $K = EI/L_0$, where EI is the bending stiffness and L_0 the length of the flexural pivot. The application of this equation requires detailed knowledge about the material properties and the geometry of the flexible segments.

The design of compliant mechanisms requires materials with a high ratio of strength to modulus R/E [1] or squared strength to modulus R^2/E [3, 4]. Fiber reinforced plastics (FRP) feature high values of R^2/E compared to other engineering materials, which makes them particularly suitable for use in high-performance compliant mechanisms. However, the manufacture of compliant mechanisms from FRP is particularly challenging due to the large difference in wall thickness between the rigid and flexible segments. The integral manufacturing of cellular FRP structures consisting of rigid cell walls connected by SLFP is possible by using a weaving process that combines terry and spacer weaving [4, 5]. However, manufacturing constraints require a transition region between both segments, resulting in a variable cross section of the flexural pivots. Additionally, the weaving process induces anisotropy due to manufacturing-specific effects such as asymmetrical layups, fiber undulations, matrix-rich transition regions with ply drop-offs, and local compaction in fiber arrangement. Both anisotropic material properties and variable cross sections must be given special consideration when modeling flexure hinges as SLFP using PRBM. Since these properties strongly depend on manufacturing, they can hardly be considered by an analytical approach. Therefore, an experimental test method is required to directly determine the bending stiffness of flexure hinges.

There are no standardized test methods for characterizing flexure hinges. Existing bending test methods involve the use of specimens with a constant thickness along the entire specimen length. However, the mechanical properties of constant cross-section specimens are not representative of the mechanical properties of thin-walled, anisotropic flexure hinges with a high thickness ratio and a transition zone. Few studies exist on the testing of flexure hinges. Smith et al. [6]

experimentally investigated circular notch and elliptical flexure hinges. The hinge stiffness was determined by applying a dead weight loading and measuring the deflection with a laser interferometer. The maximum angular deflection was set to 0.17° to limit the error caused by geometric effects. Similar experimental setups were used by Lobontiu et al. [7] investigating elliptical corner-filleted flexure hinges and by Linß et al. [8] studying semi-circular and corner-filleted flexure hinges. Zhu et al. [9] conducted fatigue tests on circular flexure hinges, while Dirkens and Lammering [10] determined natural frequencies of rectangular, circular and parabolic flexure hinges using laser scanning vibrometry. Valori et al. [11] examined injection-molded, corner-filleted flexure hinges in a test bench that applies a lateral force by pushing with a linear actuator. The test setups for flexure hinges presented in the literature are limited to small deflections or do not apply pure bending loading. There is therefore a need for test methods that can capture the large deformation bending properties of flexure hinges.

New test methods for flexure hinges are derived by adapting existing test methods for constant cross-section specimens. Tensile tests are generally not representative for the determination of flexural properties. From a physical point of view, the Young's modulus (tensile modulus) and the flexural modulus of isotropic materials are identical [12, 13]. In reality, the experimentally determined values differ slightly for plastics [14]. Moreover, tensile and flexural properties of anisotropic materials are usually not equivalent [15–17]. Flexural properties are commonly determined by three-point bending or four-point bending tests, with four-point bending tests (FPBT) having the advantage of producing a constant bending moment at the center of the specimens. However, the FPBT, as shown schematically in Fig. 2(a), applies only to small deflections [18], whereas thin-walled specimens undergo large deformations until failure. Therefore, the standardized FPBT can only be used to
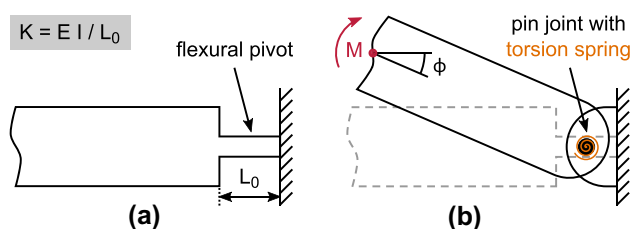

Fig. 1 Small-length flexural pivot (SLFP) with the equivalent stiffness: **a** Compliant model and **b** its representation in a pseudo-rigid-body model (PRBM)
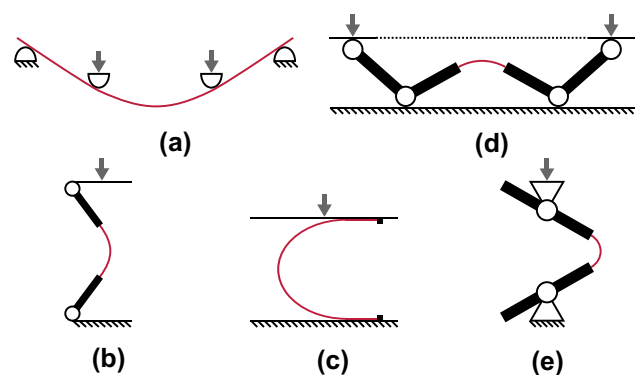

Fig. 2 Schematic representation of different bending test methods for constant cross-section specimens: **a** Four-point bending test, **b** simple vertical test, **c** platen test, **d** large deformation four-point bending test, and **e** column bending test

determine the flexural modulus of thin-walled specimens at small deflections, but not to determine the flexural properties at large deformations [19].

Various nonstandard bending test setups have been developed to account for large deformations. Simple vertical tests determine the moment–curvature curve from the post-buckling behavior under compressive loading, with both ends of the specimens attached to a universal testing machine using tapes [20, 21], plates [22], or a buckling rig [23]. The experimental setup of a simple vertical test using tapes is shown schematically in Fig. 2(b). Disadvantages of the vertical tests are gravity-induced lateral loads, leading to shear distortions of the specimens. In the platen test [24, 25], 180° bent U-shape specimens clamped between two plates are subjected to compressive loading, as shown in Fig. 2(c). However, transverse loads induce compressive strains at the specimens' midsection leading to a highly nonuniform bending moment. The platen test can be applied to determine maximum curvature at failure, but does not represent well a pure bending condition. Several research groups designed complex devices for large deformation bending tests applying pure bending loading [26–29]. In the large deformation four-point bending test (LD-FPBT) presented in [28], the specimens are clamped between two carts that rotate and translate horizontally with the crosshead displacement, shown schematically in Fig. 2(d). The LD-FPBT can accurately predict the specimens' bending stiffness. However, failure occurs due to stress concentrations at the grips, and therefore, failure properties cannot be determined.

The column bending test (CBT) [30, 31] combines the advantages of the platen test and the LD-FPBT and can simultaneously determine the specimens' stiffness and failure properties. The CBT, as shown schematically in Fig. 2(e), requires a test fixture with two rotatable fixture arms and applies a nearly pure bending loading. The mechanical properties of the specimens are determined by using a simple kinematic analysis that calculates bending moment and curvature. NASA applies the CBT to characterize thin-ply, high-strain composites for deployable booms in satellite structural applications [32, 33]. Moreover, several research groups recently utilized the CBT method. Rose et al. [34] characterized stress relaxation of thin-ply high-strain composites using a long-term CBT fixture, while Firth and Pankow [35] investigated the strain energy stored in coiled spacecraft booms by bending flattened booms. Zehnder et al. [36] used micron scale X-ray computed tomography to track the deformation of fibers in laminates at large bending deformations, and Gao et al. [19] studied the influence of temperature and asymmetric weave structure on the flexural properties of single-ply composites at large deformations. The studies of Rose et al. [37] and Long et al. [38] were on the numerical modeling of the CBT. A combined modeling and testing approach is presented by Yapa Hamillage et al. [39] evaluating the effects of weave

architecture on the relaxation response of thin-ply composites. Most recently, Aller et al. [40] investigated the bending behavior of thin composite shells with embedded fiber Bragg grating sensors using the CBT.

This paper presents novel test methods for variable cross-section flexure hinges subjected to large deformations and pure bending loading. The objective is to determine the bending stiffness of flexure hinges over their entire deflection range. The bending stiffness is required for modeling the SLFP in the PRBM, as shown in Fig. 1. The novel test methods for flexure hinges are based on the tensile test, the FPBT and the CBT, which were initially formulated for constant cross-section specimens. They are validated by comparing specimens with constant and variable cross sections and using isotropic materials with well-known properties. Anisotropy due to FRP is a comprehensive topic on its own and is not covered in this paper, but will be addressed in detail in a follow-up paper.

This paper is structured as follows: The "Materials and Methods" briefly presents the selection of test methods and test specimens investigated. The following sections "Tensile Test", "Column Bending Test" and "Four-Point Bending Test" describe the individual test methods in detail, including the experimental setup, the adaptions made for considering the shape of flexure hinges, validation by image processing, and the test results. The "Discussion" compares the different test methods and outlines limitations of each method, whereas the "Conclusion" summarizes this paper and highlights future research.

Materials and Methods

Test Methods

This study investigates flexure hinges under axial and pure bending loading. Since there are no test methods for flexure hinges subjected to large deformations, this study derives three different mechanical tests by adapting existing test methods initially formulated for constant cross-section specimens. First, tensile tests are performed as a reference. Second, an adapted CBT (aCBT) method is derived since the literature shows high potential of CBT for determining large deformation bending properties of thin-walled specimens. Finally, an adapted FPBT (aFPBT) method is derived since FPBT are commonly used and well understood.

Test Specimens

Standardized specimens and flexure hinge specimens are used in each of the three tests. Table 1 lists all types of test specimens investigated in mechanical testing.

The geometry of the flexure hinge specimens is shown in Fig. 3. While circular flexure hinges have higher precision due to a well-defined axis of rotation, corner-filleted

Table 1 Test specimens used for the different test methods

Method	Test specimens
Tensile test	Flexure hinge (according to Fig. 3)
	Dog-bone shaped (ISO 527-2, type 1B)
FPBT	Flexure hinge (according to Fig. 3)
	Rectangular plate (68 mm × 25mm × 3mm)
CBT	Flexure hinge (according to Fig. 3)
	Rectangular plate (68 mm × 25 mm × 0.5 mm)

flexure hinges enable larger deformations [6, 8]. This study investigates a modified version of a corner-filleted flexure hinge that has two opposite radii at each end. The shape of the hinge transition zone is governed by manufacturing constraints associated with integral FRP production [4, 5]. Although anisotropy is beyond the scope of this paper, the overall aim is to extend the test methodology to anisotropic materials, whereas isotropic materials are used for validation.

Standardized specimens are examined for comparison. For the tensile test, standard dog-bone shaped specimens according to ISO 527-2 [41] are used. For the FPBT and CBT, rectangular plates with the same edge dimensions as for the flexure hinges (68 mm × 25 mm) are investigated. The rectangular plates used in the FPBT have a thickness of 3 mm and comply with ISO 14125 [18], whereas the plates used in the CBT have a thickness of 0.5 mm.

Two different materials are investigated in mechanical testing: AlMg3, a metal with a distinct linear-elastic region and well-known mechanical properties, and PA6, a thermoplastic material that will also be used as the matrix component for FRP specimens in subsequent work. The specimens are manufactured by CNC milling. Six specimens per test batch are used to determine the 95 %-confidence interval (CI) of the mean value.

Tensile Test

Tensile tests are performed according to ISO 527-2 [41], examining standard dog-bone shaped specimens and flexure hinge specimens. This section presents the experimental
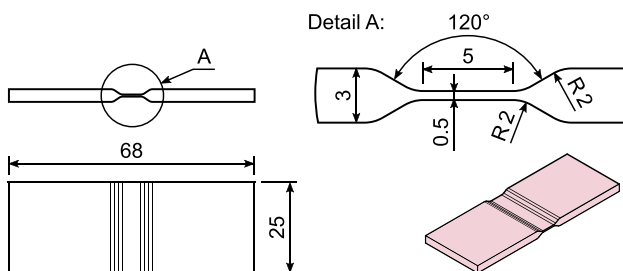
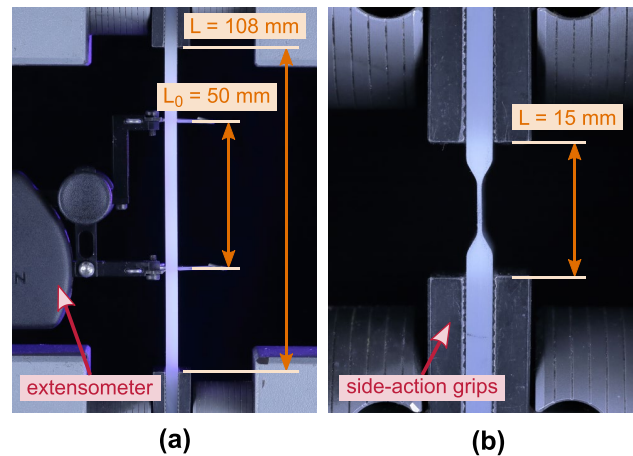**Fig. 3** Nominal dimensions of the investigated flexure hinge specimens (lengths are in mm)

Fig. 4 Tensile test setup: **a** Standard dog-bone shaped specimen according to ISO 527-2 (specimen type 1B) with extensometer. **b** Flexure hinge specimen

setup and derives two correction factors to account for the variable specimen cross section and the compliance of the test setup when using no direct strain measurement technique.

Experimental Setup

Tensile tests are conducted on a universal testing machine from the manufacturer Instron (type 5966) equipped with a 10 kN load cell. Figure 4 shows the test setup of the tensile test. The specimens are clamped using side-action grips at a constant clamping force applied with a torque wrench. The preload is approximately 1 % of the maximum load observed in preliminary tests for each specimen type.

For the standard dog-bone shaped specimens, the strain is measured directly with a mechanical clip-on extensometer with a gauge length of $L_0 = 50$ mm (type Instron 2630-111, see Fig. 4(a)). Each specimen is tested at two test speeds: A first speed to determine the Young's modulus and a second speed to determine tensile strength and strain at break. The first test speed is 1 mm min^{-1}, resulting in a strain rate of approximately 1 % min^{-1}. The second test speed is 5 mm min^{-1} and 50 mm min^{-1} for AlMg3 and PA6 specimens, respectively.

The flexure hinge specimens feature a variable cross section within the gauge length, for which there are no standardized test methods. Therefore, the test procedure of ISO 527-2 is adapted to the hinge-specific boundary conditions. Strain is calculated from crosshead displacement, since the specimen length is too short to attach a clip-on extensometer and strain gauges can interfere with the measurement when attached to small and thin-walled specimens [42]. However, to receive accurate strain values, correction factors for machine compliance and gauge length

are applied, as described subsequently. The first test speed is set to 0.125 mm min⁻¹, resulting in the same strain rate of approximately 1 % min⁻¹ as for the dog-bone shaped specimen due to the difference in gauge length. The second test speed is 0.5 mm min⁻¹ and 5 mm min⁻¹ for AlMg3 and PA6 specimens, respectively.

Correction of Machine Compliance and Gauge Length

No direct strain measurement technique is applied when testing the flexure hinge specimens. Therefore, the strain is determined from crosshead displacement. In that case, two effects have to be considered. First, the crosshead displacement ΔX is not identical to the elongation of the specimens, i.e. the increase of the gripping distance, ΔL due to compliance in the test setup. Second, the cross section and thus the strain are not uniform along the specimens' length for both the dog-bone shaped and the flexure hinge specimens. Different segments of the specimens contribute differently to the elongation ΔL, depending on the local cross-sectional area. Jia and Kagan [43] describe a method that accounts for both effects and improves the accuracy in strain measurement if the strain is calculated from crosshead displacement. This method is adapted in the current work and extended to account for the specific geometry of flexure hinge specimens.

To consider the first effect, the measured crosshead displacement

$$\Delta X = \Delta L + C_{\text{total}}P \tag{1}$$

is corrected for the total compliance C_{total} of the test setup to obtain the elongation of the specimens ΔL. The compliance of the test setup is assumed to be proportional to the load P. Figure 5(a) shows the definition of ΔX and ΔL.

The total compliance $C_{\text{total}} = C_{\text{machine}} + C_{\text{clamping}}$ is the sum of the machine compliance and the material-specific compliance within the grips. For the test setup used in this work, the machine compliance is determined experimentally to $C_{\text{machine}} = 56.6\,\mu\text{m kN}^{-1}$ using a massive steel specimen with high tensile stiffness. C_{machine} includes deformation from the load frame, the crosshead beam, the load cell, and the grips, but does not include the material-specific deformation of the specimens within the grips. Jia and Kagan [43] found that a significant part of the compliance occurs within the clamping area and depends on the specimens' Young's modulus. The total material-specific compliance is determined to $C_{\text{total,AlMg3}} = 59.7\,\mu\text{m kN}^{-1}$ and $C_{\text{total,PA6}} = 179.0\,\mu\text{m kN}^{-1}$ by comparing the crosshead deformation with the deformation measured with an extensometer on the dog-bone shaped specimens. The compliance increases with decreasing material stiffness, which is in accordance with findings presented in the literature [42, 43]. The machine compliance C_{machine} is valid
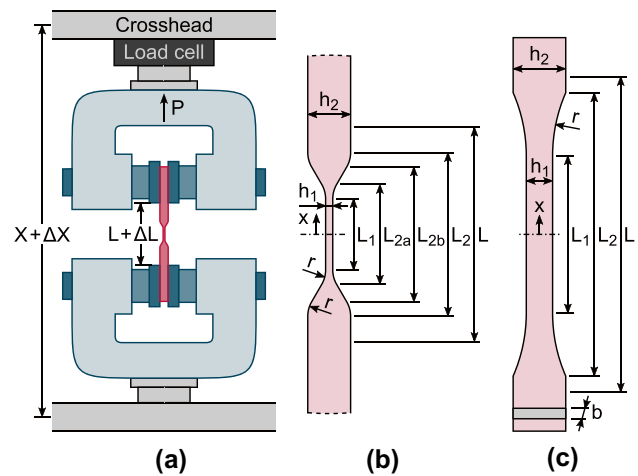

Fig. 5 Definition of geometric parameters in the tensile test: **a** Crosshead displacement ΔX and specimen elongation ΔL **b** Flexure hinge specimen. **c** Standard dog-bone shaped specimen

for the entire force range of the testing machine, whereas C_{clamping} is valid only within the linear stress–strain region.

To address the second effect, a correction factor is derived to compensate for the variable specimen cross section. The elongation

$$\Delta L = \int_{-\frac{L}{2}}^{\frac{L}{2}} \varepsilon(x)dx = 2\int_0^{\frac{L}{2}} \frac{\sigma(x)}{E}dx = \frac{2P}{Eb}\int_0^{\frac{L}{2}} \frac{dx}{h(x)} \tag{2}$$

is the integral of the strain $\varepsilon(x)$ along the length of the specimens, i.e. the initial gripping distance L, whereas the thickness $h(x)$ of the specimens is variable within the gripping distance. Equation (2) is derived using Hooke's law and is therefore restricted to the linear region of the stress–strain curve. Further, it is assumed that the stresses and strains are uniform in each cross section [43].

For determining the strain $\varepsilon_{h(x)=h_1}$ in the thin-walled center region of the variable cross-section specimen, a corrected gauge length L_0^* is defined. The corrected gauge length L_0^* is the length of an equivalent rectangular specimen with constant thickness $h(x) = h_1$ that would result in the same elongation

$$\Delta L = \varepsilon_{h(x)=h_1}L_0^* = \frac{P}{Ebh_1}L_0^* \tag{3}$$

as the actual specimens with variable thickness $h(x)$.

By comparing the right side of equation (2) and the right side of equation (3), L_0^* is determined to

$$L_0^* = 2h_1\int_0^{\frac{L}{2}} \frac{dx}{h(x)} = 2h_1\sum_i \int_{x_{l,i}}^{x_{u,i}} \frac{dx}{h_i(x)}. \tag{4}$$

To solve the integral in equation (4), the specimens are divided into segments i with the lower bound $x_{l,i}$ and

Table 2 Thickness $h_i(x)$ for each segment i relative to the symmetry plane of the specimens

Specimen	Segment$[x_{l,i}, x_{u,i}]$	Shape	Thickness$h_i(x)$
Dog-bone shaped (ISO 527-2, type 1B)[a]	$[0, L_1/2]$	constant	h_1
	$[L_1/2, L_2/2]$	circular	$-2\sqrt{r^2 - x^2} + 2r + h_1$
	$[L_2/2, L/2]$	constant	h_2
Flexure hinge[b]	$[0, L_1/2]$	constant	h_1
	$[L_1/2, L_{2a}/2]$	circular	$-2\sqrt{r^2 - x^2} + 2r + h_1$
	$[L_{2a}/2, L_{2b}/2]$	linear	$2x\dfrac{h_{2b} - h_{2a}}{L_{2b} - L_{2a}} + h_{2a}$
	$[L_{2b}/2, L_2/2]$	circular	$2\sqrt{r^2 - (x - r/2)^2} - 2r + h_2$
	$[L_2/2, L/2]$	constant	h_2

[a]$L_1 = 60\,\text{mm}, L_2 = 108\,\text{mm}, L = 108\,\text{mm}, h_1 = 10\,\text{mm}, h_2 = 20\,\text{mm}, r = 60.1\,\text{mm}, b = 4\,\text{mm}$

[b]$L_1 = 5\,\text{mm}, \quad L_{2a} = 7\,\text{mm}, \quad L_{2b} = 9.47\,\text{mm}, \quad L_2 = 11.47\,\text{mm}, \quad L = 15\,\text{mm}, \quad h_1 = 0.5\,\text{mm}, \quad h_2 = 3\,\text{mm}, r = 2\,\text{mm}, b = 25\,\text{mm}$

upper bound $x_{u,i}$, in which an analytic function for the thickness $h_i(x)$ can be derived (see Fig. 5(b), (c)). Table 2 shows the segment boundaries and piecewise-defined functions for calculating the thickness $h_i(x)$ of each segment. Only one half of the symmetrical specimens is considered, whereby $x = 0$ lies in the symmetry plane of the specimens.

The piecewise-defined integrals in equation (4) are solved numerically with global adaptive quadrature.[1] The corrected gauge length results in $L_{0,\text{dog-bone}}^* = 97.85\,\text{mm}$ and $L_{0,\text{hinge}}^* = 8.25\,\text{mm}$ for the dog-bone shaped and the flexure hinge specimens.

---

[1] For verification, the integrals in equation (4) are also solved analytically for the dog-bone shaped specimen:

$$L_0^* = L_1 + \frac{h_1}{h_2}(L - L_2) + \frac{\sqrt{h_1}}{\sqrt{h_1 + 4r}}$$

$$\left[(h_1 + 2r) \arctan\left(\frac{(h_1 + 2r)(L_2 - L_1)}{2\sqrt{h_1(h_1 + 4r)}\sqrt{r^2 - \left(\frac{L_2 - L_1}{2}\right)^2}} \right) \right.$$

$$+ (h_1 + 2r) \arctan\left(\frac{L_2 - L_1}{\sqrt{h_1(h_1 + 4r)}} \right)$$

$$\left. - \sqrt{h_1(h_1 + 4r)} \arctan\left(\frac{L_2 - L_1}{2\sqrt{r^2 - \left(\frac{L_2 - L_1}{2}\right)^2}} \right) \right]$$

The results using this analytical equation and the numerical integration of the integrals are identical. Therefore, numerical integration is suitable to avoid the tedious derivation of the analytical integrals of $h_i(x)$ for flexure hinge specimens.

In summary, by combining equations (1) and (3), the strain

$$\varepsilon = \frac{\Delta L}{L_0^*} = \frac{\Delta X - C_{\text{total}} P}{L_0^*} \tag{5}$$

is determined from crosshead displacement, corrected for both the compliance of the test setup and the variable specimen cross section. In equation (5), the crosshead displacement ΔX and the load P are directly measured by the testing machine, L_0^* is a geometry-dependent parameter, and the total compliance C_{total} is a parameter dependent on the test setup and the specimen material.

The Young's modulus is determined as the slope of the linear fit of a least-squares regression between $\varepsilon_1 = 0.05\,\%$ and $\varepsilon_2 = 0.25\,\%$ for PA6 specimens (according to ISO 527-1 [44]) and in the linear region of the stress–strain curve for AlMg3 specimens (according to method 2 in DIN EN 2002-001 [45]).

Test Results

Figure 6 shows the stress–strain curves of the dog-bone shaped specimens using different strain calculation methods.[2] The detailed view in the figure highlights the strain range used to determine the Young's modulus. The deviation between the strain $\varepsilon = \varepsilon_{\text{extensometer}}$ measured directly with an

---

[2] The stress–strain curves of the AlMg3 specimens feature oscillations occurring behind the yield point. This unstable plastic flow is typical for some alloys, including AlMg3, and is called Portevin-Le Chatelier effect [46, 47]. The instabilities caused by the Portevin-Le Chatelier effect form localized strain bands and appear as serrations in the stress–strain curve. Microscopically, the effect is based on dynamic strain aging defined by interactions between diffusing solute atoms and moving dislocations [48].
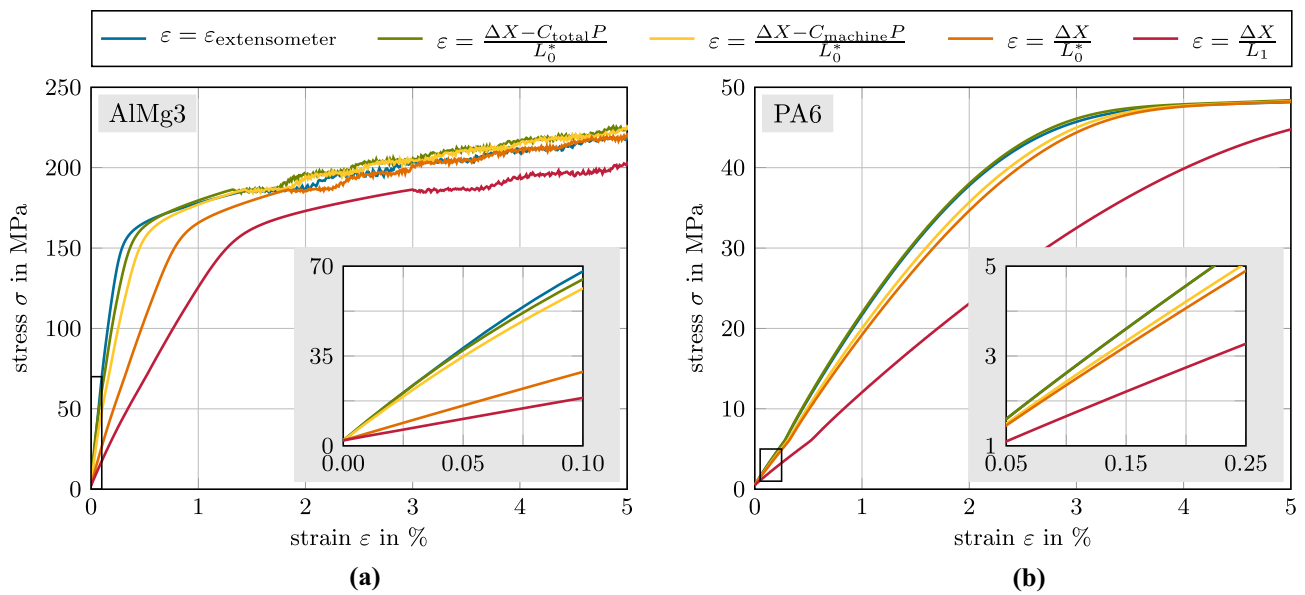
Fig. 6 Comparison of different strain calculation methods in the tensile test on standardized dog-bone shaped specimens: **a** AlMg3 and **b** PA6

extensometer and the strain $\varepsilon = \frac{\Delta X}{L_1}$ without corrections is large. Considering the corrected gauge length L_0^* and the total compliance C_{total} of the test setup, the strain $\varepsilon = \frac{\Delta X - C_{\text{total}}P}{L_0^*}$ determined from the crosshead displacement almost matches the directly measured strain $\varepsilon = \varepsilon_{\text{extensometer}}$ for both AlMg3 and PA6.

Figure 7 compares the stress–strain curves of the dog-bone shaped and the flexure hinge specimens when applying $\varepsilon = \frac{\Delta X - C_{\text{total}}P}{L_0^*}$ and $\varepsilon = \frac{\Delta X}{L_1}$. The shading indicates the 95 %-CI of the mean of each test batch. The enlarged shaded area at large strains results from material failure due to local necking of individual specimens. For both AlMg3 and PA6, the linear region in the stress–strain curves of the flexure hinge
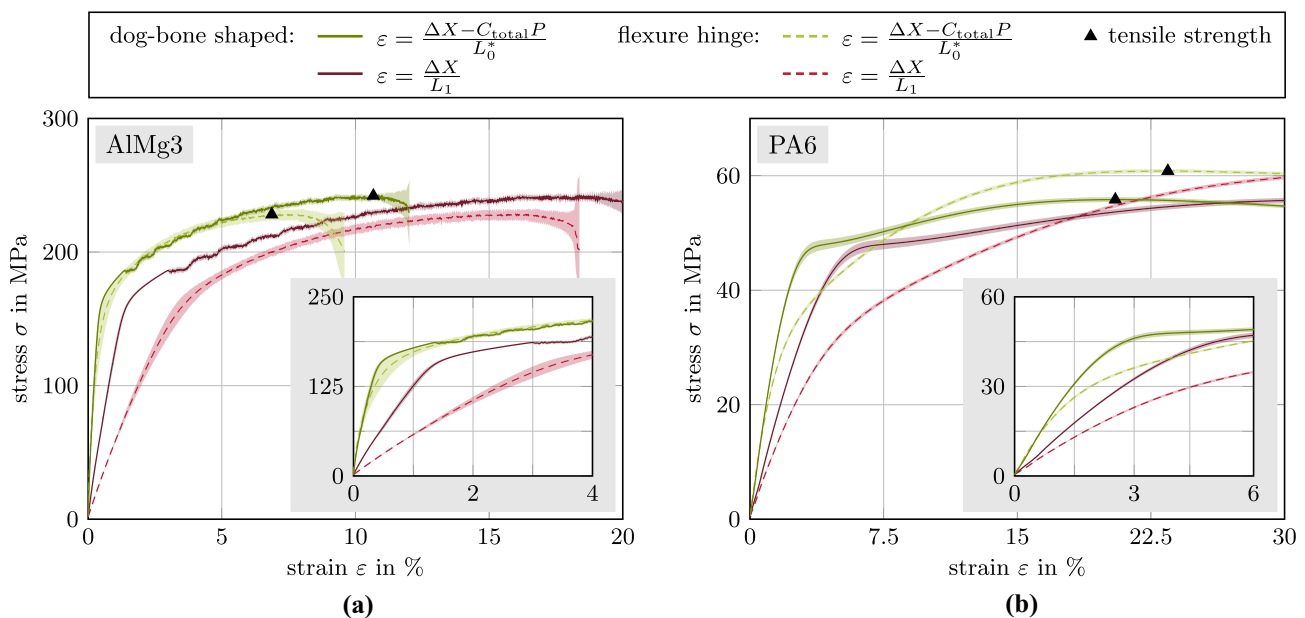
Fig. 7 Comparison of dog-bone shaped and flexure hinge specimens in the tensile test. The strain is calculated with $\varepsilon = \frac{\Delta X - C_{\text{total}}P}{L_0^*}$ and $\varepsilon = \frac{\Delta X}{L_1}$. The shading represent the 95 %-confidence interval (CI) of the mean: **a** AlMg3 and **b** PA6

specimens matches that of the dog-bone shaped specimens when both correction factors are applied (until $\varepsilon \approx 0.5\%$ for AlMg3 and $\varepsilon \approx 1\%$ for PA6), whereas the difference is large without applying the correction factors. The nonlinear region is outside the valid domain of the correction factors, but extending the method to the nonlinear region is possible by using a more complex nonlinear formulation for $\varepsilon = \varepsilon(\sigma)$ in equation (2) instead of Hooke's law.

While the corrected strain values are only valid within the linear stress–strain region, no corrections are required for the stress values, which are accurate for the entire test cycle. The tensile strength of both specimen types is marked with black triangles in Fig. 7.

Figure 8 compares the Young's modulus of the dog-bone shaped and the flexure hinge specimens using different strain calculation methods. The figure shows the effect of the individual correction factors on the Young's modulus. The effect of machine compliance is more pronounced for the AlMg3 specimens, as the applied loads are higher than for the PA6 specimens. When applying both correction factors, the modulus determined from the crosshead displacement matches between the dog-bone shaped and flexure hinge specimens, although the specimens' cross sections and the force intervals differ greatly.

Column Bending Test

Fernandez and Murphey [30] presented a novel test method for evaluating the nonlinear bending behavior of thin-ply, high-strain composites subjected to large bending deformations. The test method determines the moment–curvature relationship in the geometrically nonlinear region at large strains and is distinguished by its simplicity, as it applies a geometric closed-form solution (GCFS) solely measuring the crosshead displacement ΔX and the applied load P on a universal testing machine.

Test Method for Rectangular Plate Specimens

The CBT is a uniaxial test method using a specifically designed CBT fixture. The specimen is clamped at both ends in the fixture arms. Pin joints allow free rotation of the fixture arms. The specimen's neutral axis is slightly offset from the loading axis so that the specimen bends when an axial force is applied. Axial and shear loads are negligible compared to the bending moment, as the moment arm increases rapidly after the test begins.

Figure 9 schematically shows the CBT setup with its geometrical definitions. Herein, L_0 is the gauge length of the specimen (assumed to be constant during the test as compressive loading is negligible), $L_{a,eff}$ the effective length of the fixture arm, θ the initial angle of the fixture arm (defined by the clamping offset L_{off}), ϕ the deflection angle (change in fixture arm angle), ΔL the vertical displacement of the fixture pin joints (crosshead displacement ΔX corrected for the compliance of the test setup), P the load applied by the testing machine, and r the effective moment arm. These definitions allow the derivation of a GCFS for the bending moment and specimen curvature.

For the derivation of the GCFS, it is assumed that the curvature of the specimen is constant along the gauge length, so that the specimen forms a circular arc. In reality, the curvature is maximum at the specimen's midsection and decreases
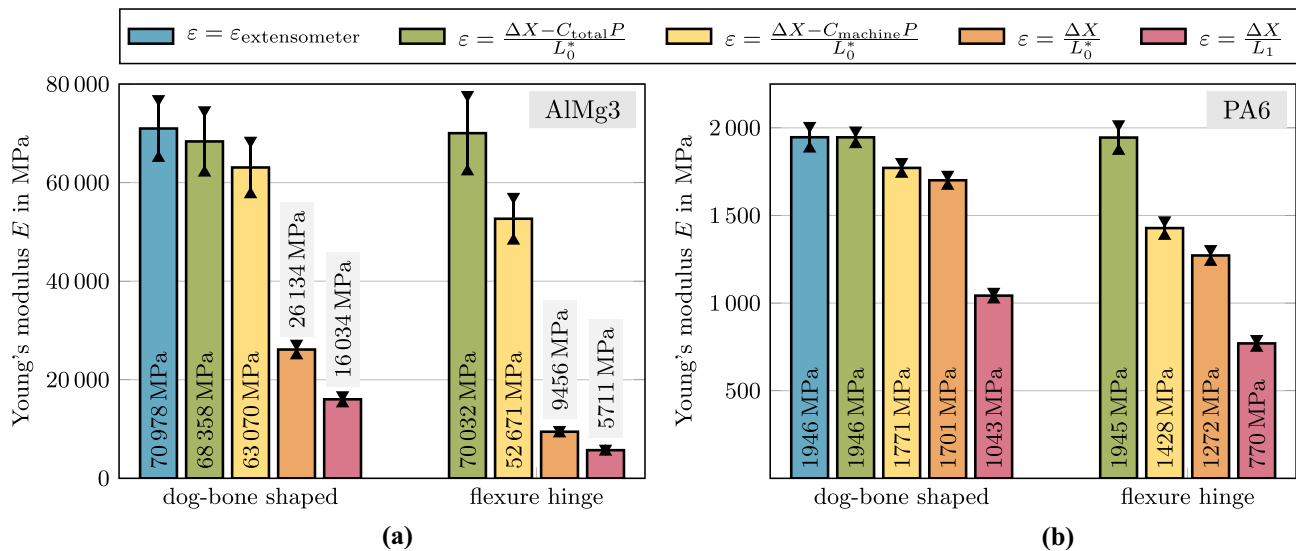

Fig. 8 Young's modulus obtained by different strain calculation methods on dog-bone shaped and flexure hinge specimens in the tensile test. Data are presented with the 95 %-CI of the mean: **a** AlMg3 and **b** PA6
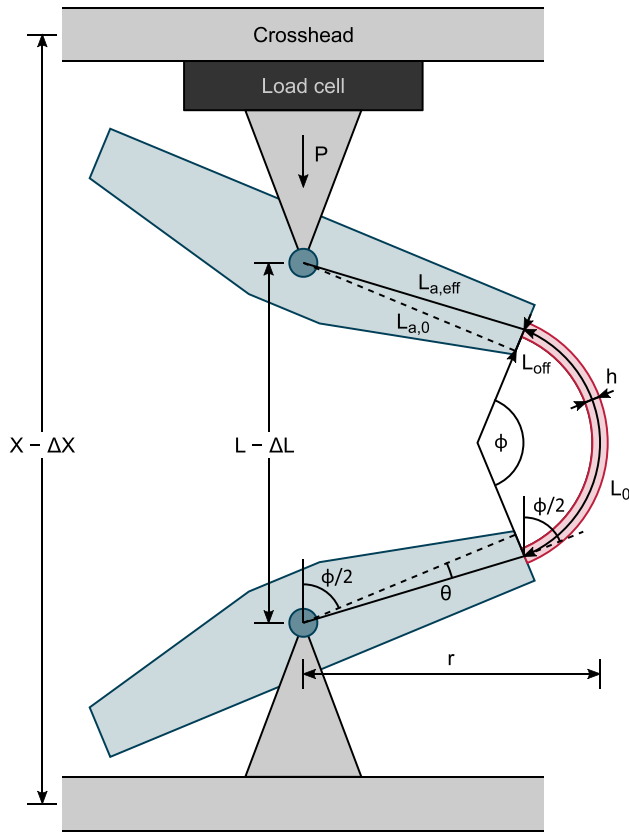
Fig. 9 Definition of angles and lengths in the column bending test (CBT)

towards the grips. However, this difference is small if the dimensions of the CBT fixture are chosen appropriately [31, 49]. The curvature κ is the reciprocal of the bending radius of a circular arc with the length L_0 and central angle ϕ. The maximum strain ε occurs on the outer surface of the specimen with the thickness h and is defined by

$$\varepsilon = \kappa \frac{h}{2} \quad \text{with} \quad \kappa = \frac{\phi}{L_0}, \qquad (6)$$

assuming the neutral axis is at the midplane of the specimen and the material behavior is linear-elastic.

The deflection angle ϕ of the fixture arms is identical to the angle of the circular arc defined by the curved specimen, as shown in Fig. 9, assuming the specimen leaves the fixture arm perpendicularly. The relationship between the angle ϕ and the vertical displacement of the fixture pin joints ΔL is geometrically defined by

$$\frac{\Delta L}{L_0} = 1 - \frac{2}{\phi} \sin \frac{\phi}{2} + 2 \frac{L_{a,\text{eff}}}{L_0} \left(\cos \theta - \cos \left(\theta + \frac{\phi}{2} \right) \right), \quad (7)$$

requiring an implicit numerical solution for ϕ [31].

The bending moment M varies linearly with the distance to the pin joints, being maximum at the specimen's midsection and decreasing towards the grips. The maximum bending moment

$$M_{max} = Pr = P \left[\frac{L_0}{\phi} \left(1 - \cos \frac{\phi}{2} \right) + L_{a,\text{eff}} \sin \left(\theta + \frac{\phi}{2} \right) \right] \tag{8}$$

at the specimen's midsection is given by the load P and the effective moment arm r. The latter is derived based on trigonometric relations (see Fig. 9 and [31]).

The bending stress given by beam theory is proportional to the bending moment. The maximum stress at the outer surface of the specimen's midsection is

$$\sigma_{max} = \frac{6M_{max}}{bh^2}. \tag{9}$$

The flexural modulus

$$E_f = \frac{\Delta M_{max}}{I \Delta \kappa} = \frac{\Delta \sigma_{max}}{\Delta \varepsilon} \tag{10}$$

is determined either from the moment–curvature curve or the stress–strain curve. The flexural modulus is calculated as the slope of the linear fit of a least-squares regression between $\varepsilon_1 = 0.05\%$ and $\varepsilon_2 = 0.25\%$ for PA6 specimens and in the linear stress–strain region for AlMg3 specimens.

Discussion of the Model Assumptions

Four recent studies evaluate the assumptions made to derive the GCFS as described above. Fernandez and Murphey [30] used digital image correlation (DIC) to evaluate the rotation angle and the strain at the tension and compression side of the specimens. The study shows good correspondence between the calculated values and the DIC results. They also compared the bending stiffness M_{max}/κ obtained from CBT with theoretical values predicted with micromechanics, resulting in a difference below 10% in most investigated cases.

Sharma et al. [31] compared the GCFS, which assumes constant curvature, with Euler's elastica theory, which can predict variable curvature along the specimen. The difference in calculated curvature between both prediction methods disappears when the specimen's gauge length L_0 is significantly shorter than the length of the fixture arms $L_{a,\text{eff}}$. The error is below 12% if $L_{a,\text{eff}}/L_0 = 1$ and below 5% if $L_{a,\text{eff}}/L_0 = 4$.

Sharma et al. [50] provide a correction factor for the curvature and bending stiffness to improve the accuracy of the GCFS. The correction factor is defined as the ratio between the exact results obtained by Euler's elastica theory and

those of the GCFS. Applying this correction factor decreases the error for $L_{a,eff}/L_0 = 0.25$ from about 20 % [31] to below 2 % [50]. The parabolic fit derived in that study is valid between $L_{a,eff}/L_0 = 0.25$ and $L_{a,eff}/L_0 = 4$.

Gao et al. [49] conducted similar investigations to Sharma et al. [31, 50] and achieved similar results. By comparing the GCFS with Euler's elastica theory, they conclude that the accuracy increases with increasing $L_{a,eff}/L_0$ and with larger offset values L_{off}. They recommend using $L_{a,eff}/L_0 > 2$, resulting in a curvature error < 5.7 % and a bending moment error < 0.32 % in that specific case.

In summary, the GCFS is accurate if the ratio $L_{a,eff}/L_0$ is appropriately chosen in the design of the CBT fixture. Otherwise, a correction factor should be applied to compensate for the nonconstant curvature caused by a small ratio of $L_{a,eff}/L_0$. In addition, Ubamanyu and Pellegrino [51] observed that the curvature error increases with smaller L_0 due to the increasing significance of edge effects.

Adapted Test Method for Flexure Hinge Specimens

Rectangular plate specimens are tested as described above, but testing flexure hinge specimens requires an adapted CBT (aCBT) method. The adaptions refer to the gauge length and the free length of the specimens.

First, the gauge length of the specimens is affected by the hinge transition zone, since some deflection occurs in the transition between the flexible and rigid segments of the specimens. A corrected gauge length L_{0f}^* is derived by defining an equivalent flexure hinge with the length L_{0f}^* and constant rectangular cross section, which has the same hinge stiffness K as the actual flexure hinge with transition zone. Paros and Weisbord [52] present expressions for determining the stiffness of single-axis and two-axis flexure hinges under combined loading by integration over the entire length of the flexure hinge. While Lobontiu et al. [53] provide closed-form equations for the stiffness factors of single-axis corner-filleted flexure hinges, Smith et al. [6] present an approximate expression for elliptical hinges subjected to pure bending loading. Assuming that the bending moment is constant over the gauge length, the bending stiffness

$$\frac{1}{K} = 2 \int_0^{\frac{L}{2}} \frac{dx}{EI(x)} = 2\frac{12}{Eb} \int_0^{\frac{L}{2}} \frac{dx}{h^3(x)} \tag{11}$$

of the flexure hinge shown in Fig. 3 is determined by integration over the length of the flexible segment with variable thickness $h(x)$.

The stiffness K of an equivalent rectangular flexure hinge with constant thickness h_1 and length L_{0f}^* is given by

$$\frac{1}{K} = \frac{12}{Ebh_1^3} L_{0f}^*. \tag{12}$$

By comparing the right side of equation (11) and the right side of equation (12), L_{0f}^* is determined in the bending case to

$$L_{0f}^* = 2h_1^3 \int_0^{\frac{L}{2}} \frac{dx}{h^3(x)} = 2h_1^3 \sum_i \int_{x_{l,i}}^{x_{u,i}} \frac{dx}{h_i^3(x)}. \tag{13}$$

Equation (13) is solved using the same procedure as in the tensile case (cf. equation (4)). The corrected gauge length results in $L_{0f,hinge}^* = 6.19$ mm by applying equation (13) to the geometric dimensions of the flexure hinge specimens given in Table 2.

The calculated value of L_{0f}^* is assessed by comparison with a finite element analysis (FEA). Therefore, the flexure hinge specimen from Fig. 3 is modeled as a three-dimensional solid structure using the simulation software ANSYS. The hinge is fixed at one end and subjected to a pure bending moment at the opposite end. The corrected gauge length determined by means of FEA is $L_{0f,hinge,FEA}^* = Ebh_1^3/12 \cdot \phi/M = 6.01$ mm, where ϕ is the angular deflection of the flexure hinge due to the applied moment M. The deviation between the value calculated by equation (13) and the value determined by FEA is less than 3 %.

Second, unlike for rectangular plate specimens, the free length of the flexure hinge specimens, i.e. the length of the specimens that is not clamped in the fixture arms, is not identical to the gauge length L_{0f}^*. Assuming that all the deformation occurs within L_{0f}^*, the remaining free length of the specimens is counted as part of the fixture arm length $L_{a,0} = (L - L_{0f}^*)/2$. Figure 10 visualizes that the modifications also affect θ and $L_{a,eff}$.
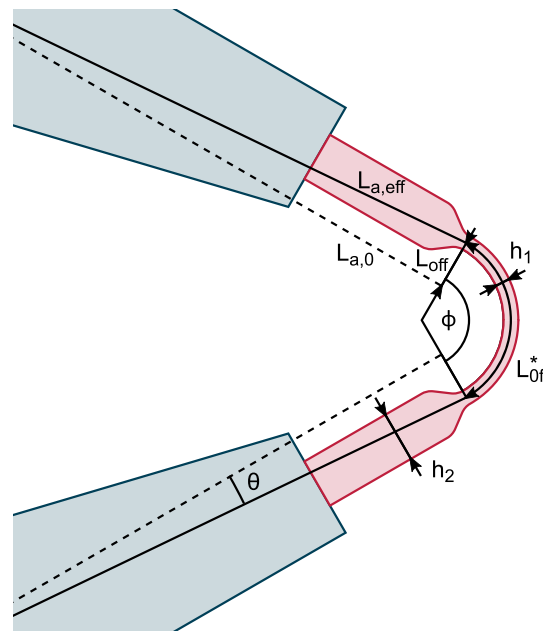

Fig. 10 Definition of geometric parameters in the adapted CBT (aCBT) on flexure hinge specimens

Experimental Setup

A universal testing machine from the manufacturer Instron (type 5567) with a 1 kN load cell is used. The CBT requires a test fixture, which is replicated by the authors of this study based on the data presented by Sharma et al. [31]. The fixture is fabricated in a stereolithography process using a *Form 2* 3D printer and the photosensitive polymer *Clear v4* from the manufacturer Formlabs. The fixture arms and the fixture frame are rotatably connected by a steel rod, with sleeve bearings reducing friction. Figure 11 shows the CBT fixture mounted in the testing machine.

The fixture arm length and the clamping offset are set to $L_{a,0} = 30$ mm and $L_{off} = 1$ mm $+ h/2$ considering the recommendations of Sharma et al. [31] and Gao et al. [49] discussed above. This results in a ratio of $L_{a,eff}/L_0 = 1.5$ for the rectangular plate specimens. When applying the aCBT method, the dimensions are $L_{a,0} = 36.9$ mm, $L_{off} = 1$ mm $+ h_2/2$ and $L_{a,eff}/L_{0f}^* = 6.0$ for the flexure hinge specimens (cf. Figs. 9 and 10). The specimens' gauge length is short compared to the length of the fixture arms, minimizing the error in curvature and bending moment caused by applying the GCFS. Gravity effects described by Fernandez and Murphey [30] can be neglected by using a counterweight-balanced test fixture [31].

Each specimen is tested at two test speeds. The first test speed is used to determine the flexural modulus and corresponds to an average strain rate of approximately 1 % min^{-1}, depending on the specimen thickness and gauge length. The test continues with a second test speed of 10 mm min^{-1} until maximum specimen deflection.

The crosshead displacement ΔX is not identical to the vertical displacement of the fixture pin joints ΔL due to compliance in the testing machine and in the CBT fixture. The compliance of the test setup shown in Fig. 11 is corrected by applying equation (1) and is determined experimentally to $C_{CBT} = 2.5$ µm N^{-1} using a steel specimen with the dimensions 69.5 mm $\times$ 25 mm $\times$ 3 mm. The bending stiffness of the steel specimen is at least two orders of magnitude larger than that of the PA6 and AlMg3 test specimens.

Instead of applying a preload, toe compensation is implemented similarly as described in ASTM D6272 [54] to account for alignment, slack, and seating of the specimens and the fixture. The toe compensation is performed by constructing a tangent to the maximum slope at the inflection point of the force–displacement curve.

Validation by Image Processing

The accuracy of the CBT and aCBT is evaluated by comparing deflections calculated by the GCFS with deflections measured by means of image processing. Images are
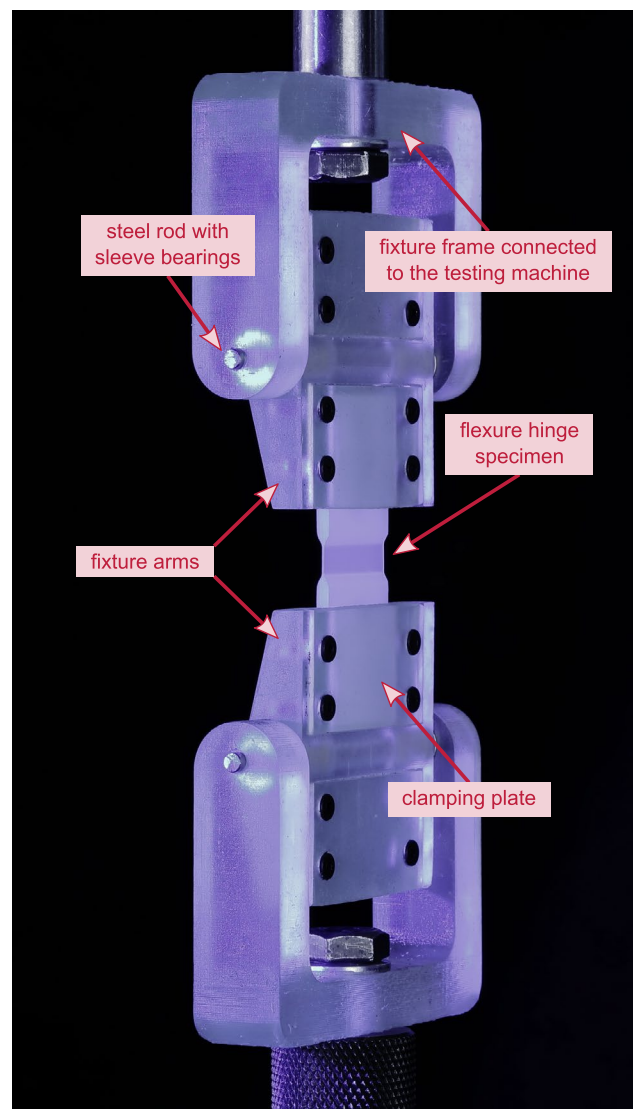

Fig. 11 CBT fixture mounted in the testing machine

captured during testing using a Canon EOS 5D Mark IV camera with a ZEISS Milvus 2/100M planar lens. Image processing determines the deflection angle ϕ, the curvature κ, and the moment arm r.

Figure 12 shows that the GCFS accurately predicts the deflection angle ϕ and the moment arm r over the entire deflection range with an error below 0.7 % and 2 % for the rectangular plate and flexure hinge specimen. Furthermore, the images confirm that the assumption of constant curvature along the specimens' gauge length is valid even at large deflections. However, the curvature κ is overpredicted by approximately 8 % for the rectangular plate specimen and underpredicted by approximately 6 % for the flexure hinge specimen.

The error in κ is likely due to a deviation in gauge length, since κ depends only on ϕ and L_0. The overprediction of κ for rectangular plate specimens implies that the specimens do not
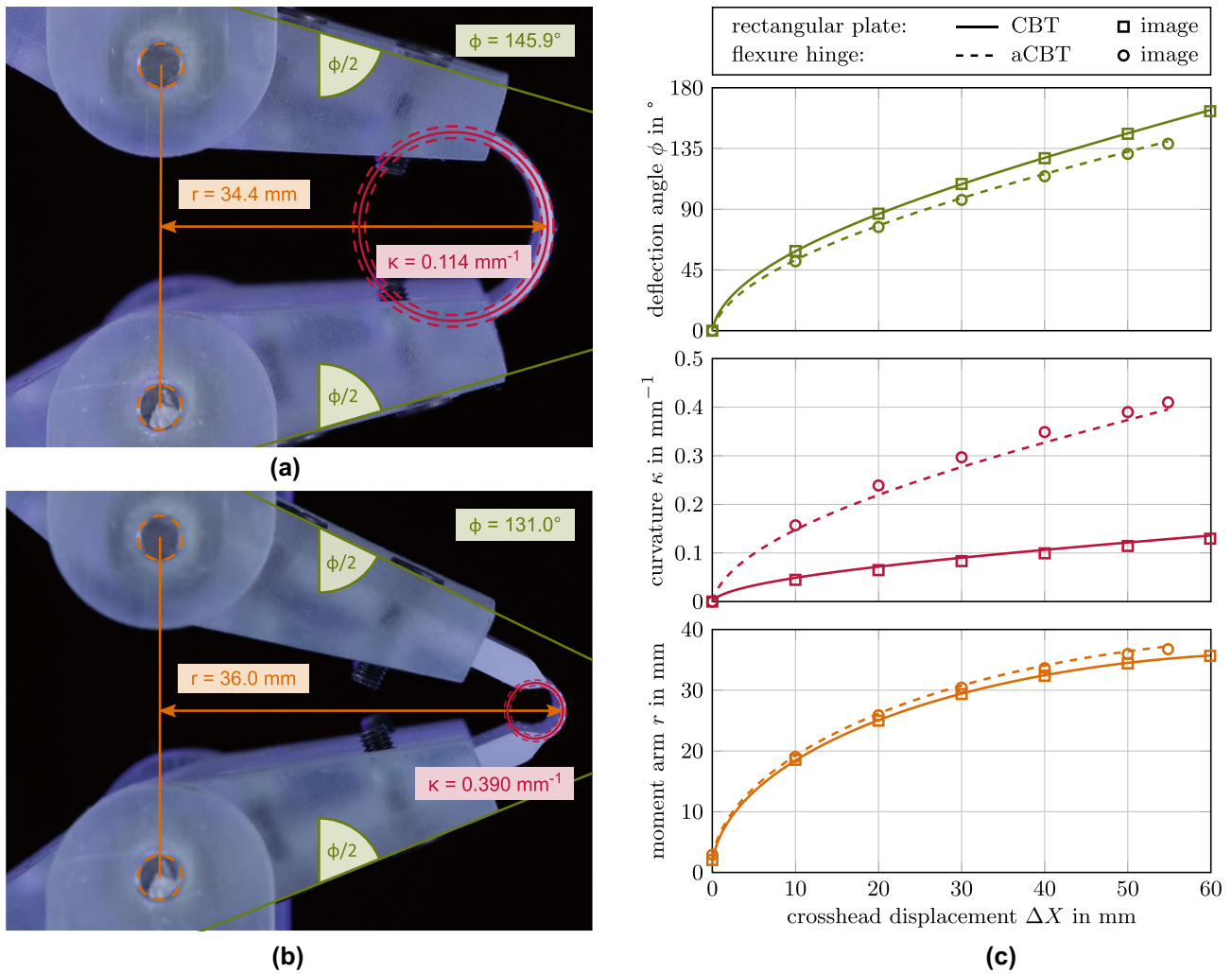
Fig. 12 Validation of the CBT and aCBT by comparing deflections calculated by the GCFS with deflections measured by image processing: **a** Rectangular plate specimen at $\Delta X = 50$ mm. **b** Flexure hinge specimen at $\Delta X = 50$ mm. **c** Deflection angle ϕ, curvature κ and moment arm r as a function of the crosshead displacement ΔX

leave the fixture arms perpendicularly and some deformation occurs within the clamping area. The compliance found for the CBT setup can be reduced by using a more rigid fixture made of metal instead of 3D-printed plastic components in future studies.

On the other hand, the underprediction of κ for flexure hinge specimens reduces from approximately 6 % to 3 % when using $L_{0f,\text{hinge,FEA}}^* = 6.01$ mm determined by means of FEA instead of $L_{0f,\text{hinge}}^* = 6.19$ mm calculated by equation (13).

The maximum curvature obtained with the used CBT setup is $\kappa = 0.14$ mm^{-1} and $\kappa = 0.40$ mm^{-1} for rectangular plate and flexure hinge specimens.

Test Results

Figure 13 compares the stress–strain curves of the rectangular plate and the flexure hinge specimens. The detailed view in

the figure shows the flexural modulus E_f for both specimen types. Failure is not observed in CBT because the materials investigated are ductile and have large strains at break.

For AlMg3 specimens, the shape of both curves is very similar, as would be expected for isotropic materials. The flexural modulus is within the 95 %-CI of the mean of the Young's modulus from the tensile test shown in Fig. 8. For PA6, the rectangular plate specimens have been excluded from this study because specimens of the desired material with the required wall thickness and geometric accuracy were not available.

The flexural modulus of the PA6 flexure hinge specimens is 19 % higher than their Young's modulus. One possible reason is friction in the fixture's bearings, which can become significant at very low loads, as in the case of PA6 (below 3 N for PA6, but up to 55 N for AlMg3 specimens). Additionally, the data of the PA6 specimens are noisy since the
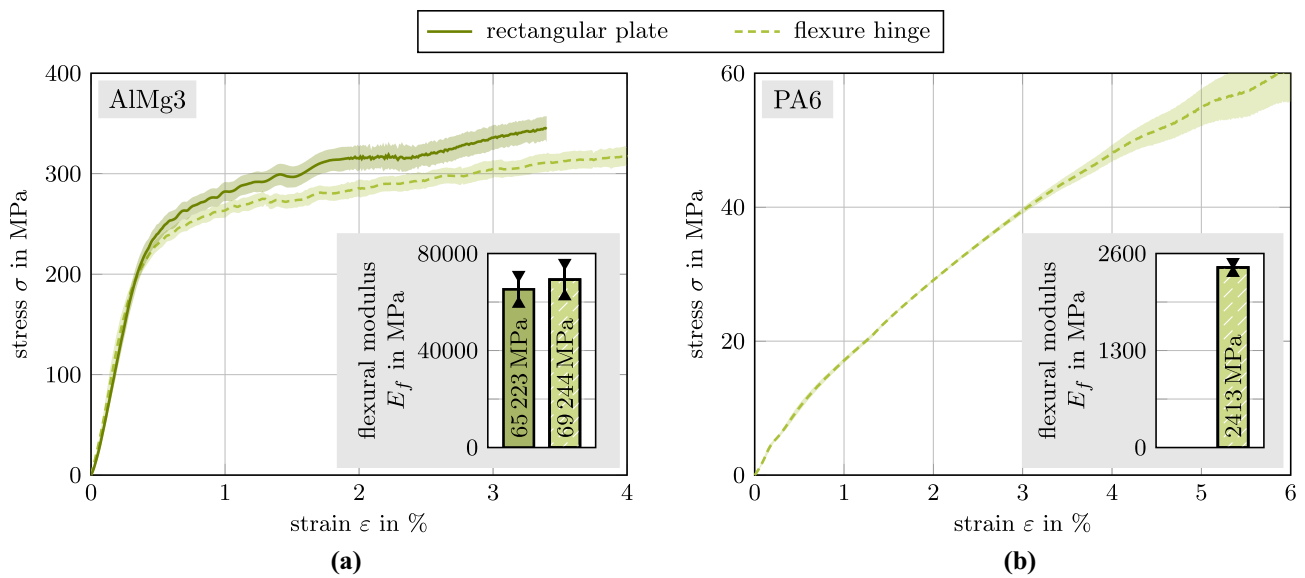
Fig. 13 Comparison of rectangular plate specimens evaluated by the CBT method and flexure hinge specimens evaluated by the aCBT method. The shaded areas represent the 95 %-CI of the mean: **a** AlMg3 and **b** PA6

applied forces are small, and not within the force range of 10 N to 1000 N to which the load cell is calibrated. Using a load cell with a lower force range is recommended to get more precise results in future studies.

Four-Point Bending Test

The standardized FPBT described in ISO 14125 [18] applies Euler-Bernoulli beam theory, which is limited to small deflections. This standardized method is extended in this study by additionally considering the variation of the contact points at large deflections, when testing rectangular plate specimens. The adapted FPBT (aFPBT) method for flexure hinges applies a GCFS that calculates the specimen's curvature from its deflection angle.

Experimental Setup

FPBT are conducted on a universal testing machine from the manufacturer Instron (type 5567) equipped with a 1 kN load cell and using a custom-made FPBT fixture. Figure 14 shows the FPBT fixture with its geometric dimensions, and the rectangular plate and flexure hinge specimen during testing. The load span and the support span are set to $L_{P,0} = 20$ mm and $L_0 = 55$ mm, and the radii at loading noses and supports are $r_{inner} = 3$ mm and $r_{outer} = 5$ mm, respectively. A deflectometer measures the midspan deflection s relatively to the loading noses.

Each specimen is tested at two test speeds. The first one is used to determine the flexural modulus and

corresponds to a strain rate of approximately 1 % min^{-1}, depending on the specimen thickness and gauge length. The test continues with a second test speed of 5 mm min^{-1} until maximum specimen deflection. The preload is approximately 1 % of the maximum load observed in pretests for each specimen type.

The crosshead displacement ΔX is not identical to the vertical displacement of the loading noses due to compliance in the testing machine and in the FPBT fixture. The compliance of the test setup shown in Fig. 14 is corrected by applying equation (1) and is determined experimentally to $C_{FPBT} = 0.15\,\mu m\,N^{-1}$ using a massive steel specimen with the cross-sectional dimensions of 50 mm × 14.9 mm.

Test Method for Rectangular Plate Specimens Considering the Variation of the Contact Points

The standardized FPBT method assumes that the contact points remain constant during the test. However, the loading noses and supports of the FPBT fixture are not sharp but have a radius, resulting in a variation of the contact points between fixture and specimen as the specimen deflects. As a result of horizontal displacements, the support span L and external span L_A decrease, and the load span L_P increases. Vertical displacements reduce the effective crosshead displacement ΔX_e. Figure 15 shows the effects of horizontal and vertical displacements that are calculated using equations (14)–(16).

$$L_A = L_{A,0} - r_{inner} \sin(\alpha_{inner}) - r_{outer} \sin(\alpha_{outer}) \tag{14}$$
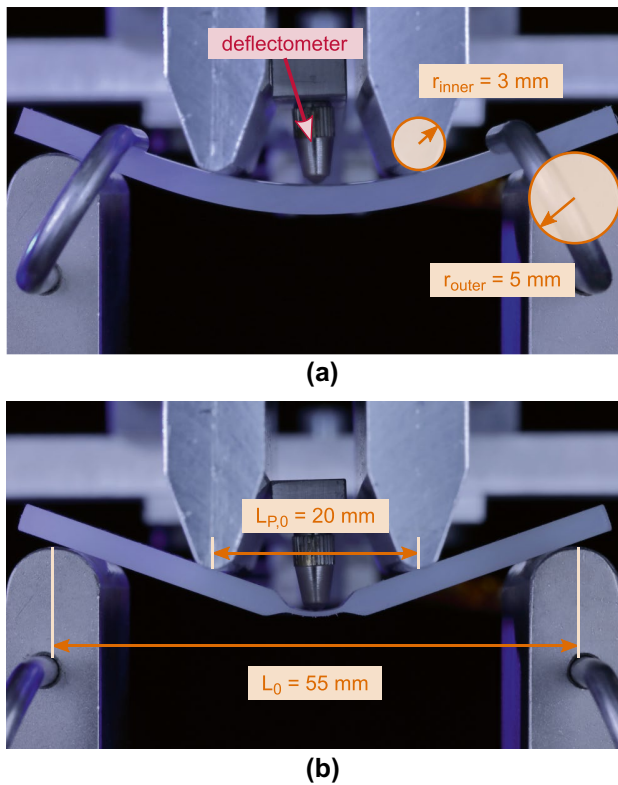
(a)

(b)

Fig. 14 Four-point bending test (FPBT) setup: **a** Rectangular plate specimen according to ISO 14125. **b** Flexure hinge specimen

$$L_P = L_{P,0} + 2r_{inner} \sin(\alpha_{inner}) \tag{15}$$

$$\begin{aligned} \Delta X_e = {} & \Delta X - r_{inner}(1 - \cos(\alpha_{inner})) \\ & - r_{outer}(1 - \cos(\alpha_{outer})) \end{aligned} \tag{16}$$

Rectangular plate specimens are tested according to ISO 14125 [18], assuming the deflection curve w is described by an Euler-Bernoulli beam. The angles α_{inner} and α_{outer} are obtained from the first derivative $w' = -\tan(\alpha)$ of the beam's deflection curve:

$$\begin{aligned} \alpha_{inner} &= \arctan\left(\frac{3P}{Ebh^3}L_A L_P\right) \\ &= \arctan\left(\frac{L_P}{h}\varepsilon\right) \end{aligned} \tag{17}$$

$$\begin{aligned} \alpha_{outer} &= \arctan\left(\frac{3P}{Ebh^3}\left(L_A^2 + L_A L_P\right)\right) \\ &= \arctan\left(\frac{L_A + L_P}{h}\varepsilon\right) \end{aligned} \tag{18}$$

Equations (17) and (18) are simplified with $\varepsilon = \sigma/E = 3PL_A/(Ebh^2)$ [55]. The calculation of the
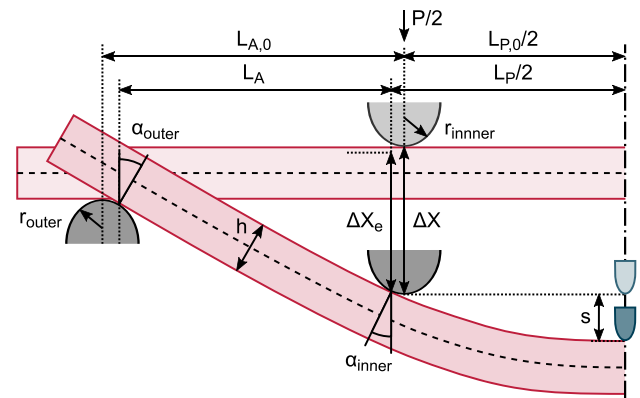
Fig. 15 Definition of geometric parameters in the FPBT on rectangular plate specimens, including horizontal and vertical displacements due to the variation of the contact points. The figure shows one half of the symmetrical test setup

deflection angles requires an implicit numerical solution, as L_A and L_P depend on α_{inner} and α_{outer}. In contrast, Mujika et al. [55] consider the variation of the contact points by assuming small deflections ($\sin(\alpha) \approx \alpha$ and $\tan(\alpha) \approx \alpha$), which allows for an explicit solution of α_{inner} and α_{outer}.

For rectangular plate specimens, the flexural modulus

$$E_f = \frac{L_A}{4bh^3}(4L_A(2L_A + 3L_P) + 3L_P^2)\frac{\Delta P}{\Delta X + \Delta s} \tag{19}$$

is determined by deriving the deflection curve of an Euler-Bernoulli beam using the corrected span values.

Adapted Test Method for Flexure Hinge Specimens

When comparing flexure hinge specimens to rectangular plate specimens, the deformation of the flexure hinge is concentrated on the flexible segment, whereas the outer segments are assumed to be rigid. Therefore, the equations given by the standardized FPBT method [18] using Euler-Bernoulli beam theory are not applicable for flexure hinge specimens. Figure 16 shows the deflected flexure hinge specimen and the definition of relevant geometric parameters. A new system of equations must be defined to determine the stress–strain curve of the flexure hinge.

The aFPBT method applies the same assumptions made to derive the GCFS used in the aCBT. When assuming constant curvature along the specimen's gauge length, the specimen forms a circular arc with the length L_{0f}^* and central angle ϕ, as shown in Fig. 16. Applying equation (6) results in

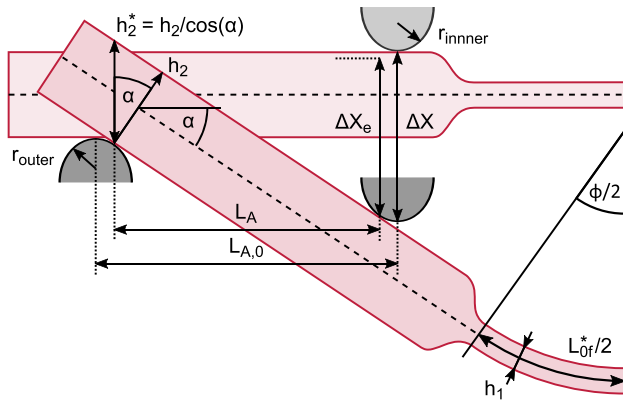$$\kappa = \frac{\phi}{L_{0f}^*} = \frac{2\alpha}{L_{0f}^*}. \tag{20}$$

Fig. 16 Definition of geometric parameters in the adapted FPBT (aFPBT) on flexure hinge specimens. The figure shows one half of the symmetrical test setup

The length L_{0f}^* of the flexible segment is given by equation (13), similar to the aCBT. The angle ϕ of the circular arc is equal to twice the deflection angle α. Since no deflection of the specimen occurs between the supports and loading noses, the inner and the outer deflection angle are identical: $\alpha_{inner} = \alpha_{outer} = \alpha$. The deflection angle

$$
\begin{aligned}
\alpha &= \arctan\left(\frac{\Delta X_e + h_2^* - h_2}{L_A}\right) = \arctan\left(\frac{\Delta X_e + h_2\left(\frac{1}{\cos(\alpha)} - 1\right)}{L_A}\right) \\
&= \arctan\left(\frac{\Delta X - (r_{inner} + r_{outer})(1 - \cos(\alpha)) + h_2\left(\frac{1}{\cos(\alpha)} - 1\right)}{L_{A,0} - (r_{inner} + r_{outer})\sin(\alpha)}\right)
\end{aligned}
$$

(21)

is geometrically defined (see Fig. 16), but its calculation requires an implicit numerical solution.

Unlike the standardized FPBT described in ISO 14125, the aFPBT requires only the crosshead displacement ΔX and the applied load P as input data recorded by the universal testing machine, and is independent of the midspan deflection s measured by the deflectometer. Furthermore, the evaluation of the aFPBT does not apply Euler-Bernoulli beam theory, which is limited to small deflections. The GCFS used in the aFPBT is geometrically defined and is also valid for large deformations. However, for large deformations, other sources of deviations occur that have not been considered so far, such as friction [56, 57] and horizontal forces [55].

Validation by Image Processing

Image processing determines the deflection angle α and the curvature κ for both specimen types. Figure 17 compares the calculated deflections with the deflections measured by means of image processing. The image processing shows

that the test methods predict the deflection angle α and the curvature κ accurately for small crosshead displacements with an error below 2.5 % and 1 % for the rectangular plate and flexure hinge specimen.

However, the error between the calculated values and those measured by means of image processing increases for displacements $\Delta X > 7.5$ mm. The error at large deflections is higher for the rectangular plate specimen (28.9 % at $\Delta X = 15$ mm) than for the flexure hinge specimen (4.3 % at $\Delta X = 15$ mm), since Euler-Bernoulli beam theory is limited to small deflections. The findings are in accordance with ISO 14125 [18] that recommends a large deflection correction for deflections larger than 10 % of the support span, i.e. 5.5 mm in this particular case. The correction factor given in ISO 14125 is, however, limited to the specific experimental setup and specimen geometry defined therein and cannot be applied to other test setups.

The displacement of $\Delta X = 7.5$ mm is set as the limit of the presented FPBT setup. The curvature at this displacement is $\kappa = 0.03$ mm^{-1} and $\kappa = 0.15$ mm^{-1} for rectangular plate and flexure hinge specimens.

Test Results

Figure 18 compares the stress–strain curves of the rectangular plate and the flexure hinge specimens.[3] The detailed view in the figure shows the flexural modulus E_f for both specimen types. The stress–strain curves of the rectangular plate specimens using Euler-Bernoulli beam theory and the curves of the flexure hinge specimens using a GCFS have the same shape at small deflections but show deviations at large deflections.

In the FPBT, no failure characteristics can be determined for thin-walled specimens, since the specimens undergo large deformations until failure. However, the validity of standardized bending test procedures is limited to small deflections. ISO 178 [13] specifies a conventional deflection of $s_c = 1.5h$ as a limit for the standardized bending test. The strain at the conventional deflection is $\varepsilon_{sc,plate} \approx 2.3$ % and $\varepsilon_{sc,hinge} \approx 0.37$ % for the rectangular plate and flexure hinge specimens, shown in Fig. 18 with vertical dotted lines. Since the GCFS applied for flexure hinge specimens is also valid for large deflections, $\varepsilon_{sc,hinge}$ does not represent a limit for the aFPBT.

Discussion

Compliant mechanisms can be analyzed by using PRBM. PRBM represent flexible segments by discrete pin joints and torsion springs with the stiffness $K = EI/L_0$. This study

---

[3] The test of the AlMg3 rectangular plate specimens stopped at $\varepsilon \approx 0.5$ % when reaching the 1 kN force limitation of the load cell.
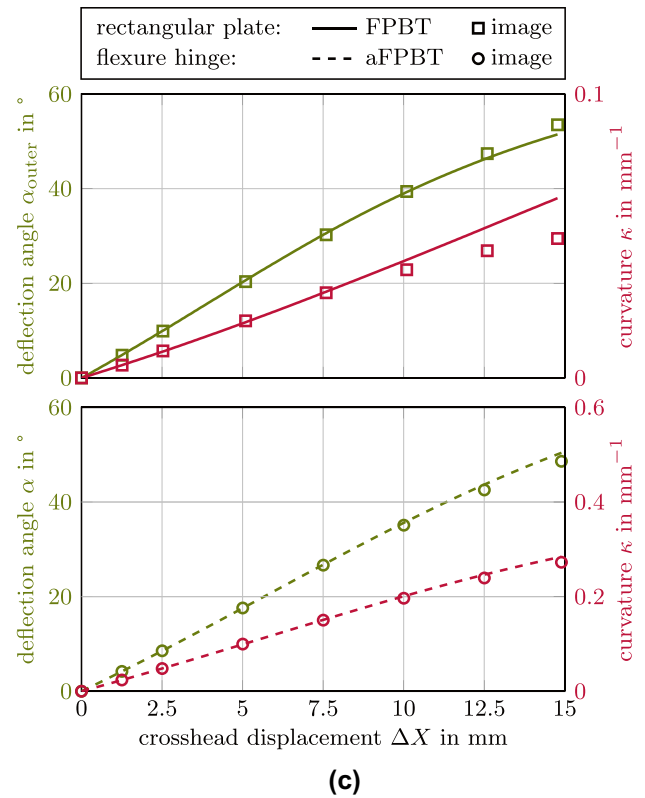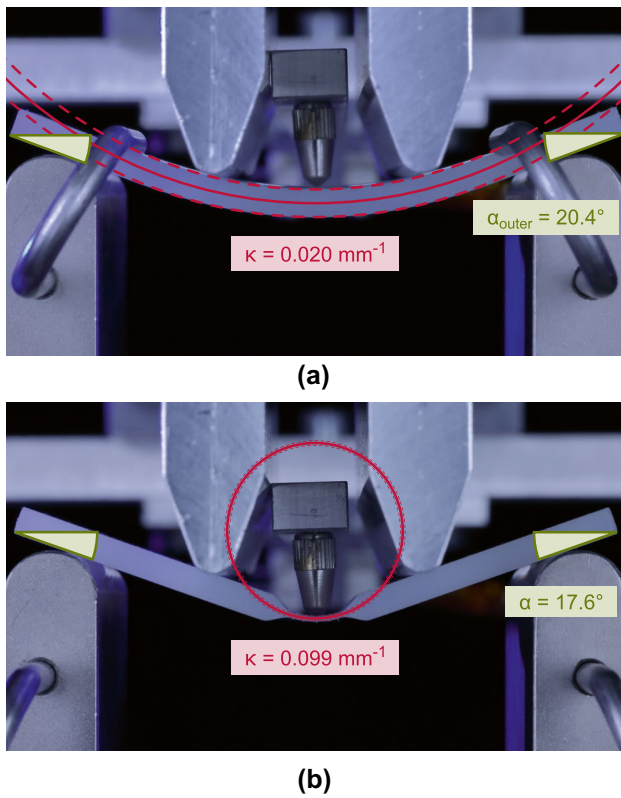
Fig. 17 Validation of the FPBT and aFPBT by comparing the deflections calculated by Euler-Bernoulli beam theory and the GCFS with deflections measured by image processing: **a** Rectangular plate specimen at $\Delta X = 5$ mm. **b** Flexure hinge specimen at $\Delta X = 5$ mm. **c** Deflection angle α and curvature κ as a function of the crosshead displacement ΔX

describes methods for determining EI and L_0 for flexure hinges with variable cross section. While the bending stiffness EI is determined experimentally, the specimen's gauge length L_0 is defined by the geometry of the flexible segment.

This paper takes into account the variable cross section of flexure hinges by introducing a corrected gauge length L_0^*. The investigated flexure hinge consists of a flexible segment with constant thickness and a transition zone with variable
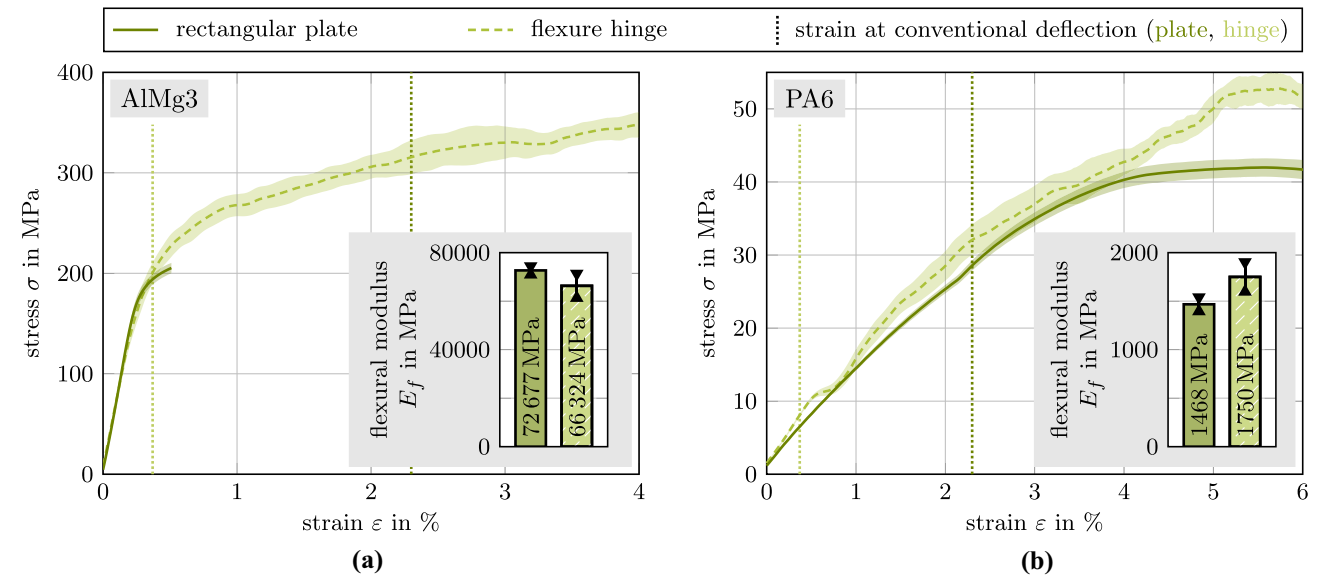
Fig. 18 Comparison of rectangular plate specimens evaluated by the FPBT method and flexure hinge specimens evaluated by the aFPBT method. The shaded areas represent the 95 %-CI of the mean: **a** AlMg3 and **b** PA6

thickness defined by manufacturing constraints (cf. Fig. 3). The corrected gauge length is defined as the length of an equivalent rectangular specimen with constant cross section that has the same hinge stiffness K as the actual flexure hinge with transition zone. A set of analytical equations is defined determining the corrected gauge length to $L_{0,hinge}^{*} = 8.25$ mm and $L_{0f,hinge}^{*} = 6.19$ mm for the flexure hinge subjected to tensile and bending loading. When comparing both values with the length $L_1 = 5$ mm of the rectangular segment of the flexure hinge and the length $L_2 = 11.47$ mm of the flexure hinge including the transition zone, the corrected gauge length is in between L_1 and L_2. The influence of the transition zone with gradually increasing thickness is more pronounced in the case of tensile loading, because tensile stiffness depends linearly on the specimen's thickness and bending stiffness cubically. Verification shows that the error between $L_{0f,hinge}^{*} = 6.19$ mm and $L_{0f,hinge,FEA}^{*} = 6.01$ mm determined by means of FEA is less than 3 %.

The bending stiffness EI of the flexure hinge is determined experimentally instead of calculating it from the Young's modulus E and the second moment of area I to include manufacturing-specific effects. Two bending test methods for flexure hinges are derived by adapting the FPBT and CBT. While the standardized FPBT applies Euler-Bernoulli beam theory to examine specimens with constant cross section, the aFPBT applies a GCFS investigating flexure hinge specimens. Compared to Euler-Bernoulli beam theory, the GCFS is not limited to small deflections. However, for large deflections, effects such as friction and horizontal forces become significant that are not covered by the aFPBT. In contrast, the CBT is designed for determining pure bending properties at large curvatures. With the presented test setup, the aCBT is accurate even at large deflections and achieves a curvature of up to $\kappa = 0.40$ mm^{-1}, whereas the maximum curvature in the aFPBT is limited by the test methodology to about $\kappa = 0.15$ mm^{-1}.

The aFPBT and aCBT presented in this paper are limited to flexure hinge specimens that consist of a geometrically defined transition region and a segment with constant thickness at the center of the specimens, since equations (6) and (20) assume constant curvature. Image processing confirms that the assumption of constant curvature is met for both the aFPBT and aCBT for the flexure hinge investigated, which is similar to a corner-filleted flexure hinge with two opposite radii at each end. For other types of flexure hinges, such as circular and elliptical hinges, the assumption of constant curvature is not satisfied. Though, any type of flexure hinge could be characterized with the proposed aFPBT and aCBT methods using a more complex experimental setup where the strain is measured with DIC rather than calculated with the equations provided in this paper. Nevertheless, the approach

of defining a corrected gauge length L_0^{*} applies to arbitrary geometries in tensile and bending testing. Moreover, the test methods presented for flexure hinges are distinguished by their simplicity, since they require only the measurement of the crosshead displacement ΔX and the applied load P on a universal testing machine.

For comparison, a tensile test method is presented to determine the Young's modulus and the tensile strength of variable cross-section specimens without using a direct strain measurement technique. By considering the corrected gauge length L_0^{*} and the total compliance C_{total} of the test setup, the strain calculated from crosshead displacement matches the strain directly measured with an extensometer in the linear region of the stress–strain curve. The method applies to specimens of any shape as long as the shape is defined by analytical equations.

When comparing all three test methods and when comparing flexure hinge specimens with constant cross-section specimens, the test results are in good accordance in the linear stress–strain region. Figure 19 compares the modulus of elasticity determined with all three test methods on flexure hinge specimens. For AlMg3, the flexural modulus determined in the aCBT and aFPBT differs by less than 5 % from the Young's modulus determined in the tensile test, which is to be expected from a physical point of view.

Material properties of plastics are more variable and less predictable than those of metals [1]. The flexural modulus of PA6 determined in the aFPBT is about 10 % lower than the Young's modulus, which is in accordance with data presented in the literature [58] and with most material data sheets provided by various manufacturers. The flexural modulus determined in the aCBT is about 19 % higher than the Young's modulus, contrary to expectation. This is possibly due to friction in the fixture's bearings, which can become significant at very low loads, as in the case of PA6. Therefore, the authors recommend using ball bearing instead of plain bearings in the CBT fixture when testing specimens with very low bending stiffness.

While the results presented in this paper show the stress–strain curves of all specimens to allow comparison between tensile and bending tests, the PRBM requires the hinge stiffness K as an input parameter for designing compliant mechanisms. The hinge stiffness can either be calculated via $K = EI/L_0$ or determined experimentally in the aCBT or aFPBT from the slope of the moment–deflection curve with $K = M/\phi$. Whereas the stiffness calculation is accurate for hinges made of isotropic materials, this is not the case when material inhomogeneities are present as in anisotropic flexure hinges made of FRP. With the methodology presented in this paper, the hinge stiffness can be experimentally determined over the entire deflection range of flexure hinges of any material.
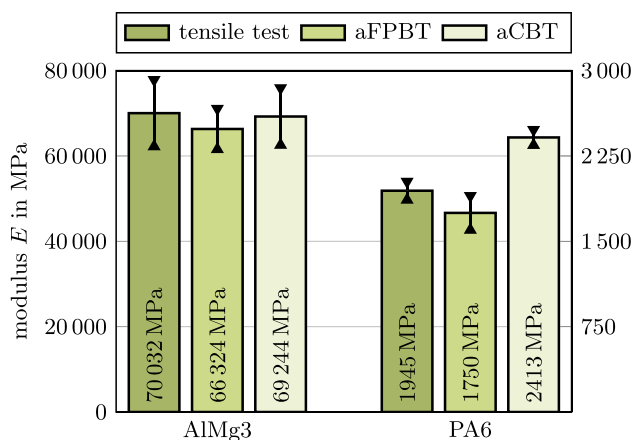
Fig. 19 Modulus of elasticity determined on flexure hinge specimens by different test methods. Data are presented with the 95 %-CI of the mean

Conclusion

Compliant mechanisms offer many advantages over conventional rigid-body mechanisms, but their design and analysis are much more challenging. Modeling compliant mechanisms requires detailed knowledge about the material properties and the geometry of their flexible segments. This study derived three test methods for characterizing flexure hinges subjected to axial and pure bending loading by adapting tensile test, FPBT and CBT.

The investigated flexure hinge features a variable cross section with a transition zone governed by manufacturing constraints. In this paper, the variable cross section of flexure hinges is taken into account by introducing a corrected gauge length L_0^*. The corrected gauge length is determined for the case of pure axial and pure bending loading.

The newly derived bending test methods for flexure hinges are adaptations of the standardized FPBT and the CBT. These test methods were initially formulated for constant cross-section specimens, but are adapted in this study to examine variable cross-section specimens. The moment–curvature relationship of the specimens is determined using a GCFS that calculates the curvature from the angular deflection of the flexure hinge. The derived test methods are validated by comparing the calculated specimen deflections with those measured by image processing. While the aCBT proves to be a suitable test method for flexure hinges at large deflections, the stiffness characterization at small deflections can be performed either with the aCBT or the aFPBT. Therefore, the presented aCBT and aFPBT methods validated on isotropic materials form the basis for characterizing anisotropic flexure hinges.

Future research will incorporate the development of integrally woven cellular FRP structures consisting of rigid cell walls connected by flexure hinges to realize efficient morphing structures for aeronautical applications. Pressure-actuated cellular structures allow high structural deformations while simultaneously having high load-bearing capacity, which is a prerequisite for actuated adaptive wingtips [59, 60] or morphing ailerons [61]. The extension of the presented test methods for the characterization of anisotropic flexure hinges enables high-performance compliant mechanisms made from FRP.

Declarations

References

1. Howell LL (2001) Compliant Mechanisms. Wiley, New York
2. Howell LL, Midha A (1994) A Method for the Design of Compliant Mechanisms With Small-Length Flexural Pivots. J Mech Des. 116(1):280–290. https://doi.org/10.1115/1.2919359
3. Gramüller B, Boblenz J, Hühne C (2014) PACS–Realization of an adaptive concept using pressure actuated cellular structures. Smart Mater Struct. 23(11):115006. https://doi.org/10.1088/0964-1726/23/11/115006
4. Meyer P, Boblenz J, Sennewald C, Vorhof M, Hühne C, Cherif C et al (2019) Development and Testing of Woven FRP Flexure Hinges for Pressure-Actuated Cellular Structures with Regard to Morphing Wing Applications. Aerospace. 6(11):116. https://doi.org/10.3390/aerospace6110116
5. Vorhof M, Sennewald C, Schegner P, Meyer P, Hühne C, Cherif C et al (2021) Thermoplastic Composites for Integrally Woven Pressure Actuated Cellular Structures: Design Approach and Material Investigation. Polymers. 13(18):3128. https://doi.org/10.3390/polym13183128

6. Smith ST, Badami VG, Dale JS, Xu Y (1997) Elliptical flexure hinges. Rev Sci Instrum. 68(3):1474–1483. https://doi.org/10.1063/1.1147635

7. Lobontiu N, Cullin M, Ali M, Brock JMF (2011) A generalized analytical compliance model for transversely symmetric three-segment flexure hinges. Rev Sci Instrum. 82(10):105116. https://doi.org/10.1063/1.3656075

8. Linß S, Schorr P, Zentner L (2017) General design equations for the rotational stiffness, maximal angular deflection and rotational precision of various notch flexure hinges. Mech Sci. 8(1):29–49. https://doi.org/10.5194/ms-8-29-2017

9. Zhu B, Lu Y, Liu M, Li H, Zhang X (2018) Fatigue study on the right circular flexure hinges for designing compliant mechanisms. In: ASME 2017 International Mechanical Engineering Congress and Exposition. Fairfield, New York: Am Soc Mech Eng. https://doi.org/10.1115/IMECE2017-70853

10. Dirksen F, Lammering R (2011) On mechanical properties of planar flexure hinges of compliant mechanisms. Mech Sci. 2(1):109–117. https://doi.org/10.5194/ms-2-109-2011

11. Valori M, Surace R, Basile V, Luzi L, Vertechy R, Fassi I (2020) Rapid fabrication of POM flexure hinges via a combined injection molding and stereolithography approach. In: ASME 2020 International Design Engineering Technical Conferences and Computers and Information in Engineering Conference. Fairfield, New York: Am Soc Mech Eng. https://doi.org/10.1115/DETC2020-22476

12. Jaroschek C (2012) The end of the flexural modulus. J Plast Technol. 8(5):515–524

13. DIN EN ISO 178 (2019) Plastics – Determination of flexural properties (ISO 178:2019) German version EN ISO 178:2019

14. Harper CA (ed) (1999) Modern Plastics Handbook. McGraw-Hill, New York

15. Tsai SW, Hahn HT (1980) Introduction to Composite Materials. Technomic Publishing Company, Lancaster, Pennsylvania

16. Mallikarachchi HMYC, Pellegrino S (2013) Failure criterion for two-ply plain-weave CFRP laminates. J Compos Mater. 47(11):1357–1375. https://doi.org/10.1177/0021998312447208

17. Gao J, Chen W, Yu B, Fan P, Zhao B, Hu J et al (2019) A multi-scale method for predicting ABD stiffness matrix of single-ply weave-reinforced composite. Compos Struct. 230:111478. https://doi.org/10.1016/j.compstruct.2019.111478

18. DIN EN ISO 14125 (2011) Fibre-reinforced plastic composites – Determination of flexural properties (ISO 14125:1998 + Cor.1:2001 + Amd.1:2011); German version EN ISO 14125:1998 + AC:2002 + A1:2011

19. Gao J, Chen W, Chen J, Hu J, Zhao B, Zhang D et al (2021) Large deformation bending of single-ply fabric reinforced polymer composite. Polym Compos. 42(11):6038–6050. https://doi.org/10.1002/pc.26283

20. Yee JCH, Pellegrino S (2005) Folding of woven composite structures. Compos A Appl: Sci: Manuf 36(2):273–278. https://doi.org/10.1016/j.compositesa.2004.06.017

21. López Jiménez F, Pellegrino S (2012) Folding of fiber composites with a hyperelastic matrix. Int J Solids Struct. 49(3–4):395–407. https://doi.org/10.1016/j.ijsolstr.2011.09.010

22. Kwok K, Pellegrino S (2013) Folding, Stowage, and Deployment of Viscoelastic Tape Springs. AIAA J. 51(8):1908–1918. https://doi.org/10.2514/1.J052269

23. Wisnom MR, Atkinson JW (1997) Constrained buckling tests show increasing compressive strain to failure with increasing strain gradient. Compos A Appl: Sci: Manuf 28(11):959–964. https://doi.org/10.1016/S1359-835X(97)00067-5

24. Yee JCH, Pellegrino S (2005) Biaxial bending failure locus for woven-thin-ply carbon fibre reinforced plastic structures. In: 46th AIAA/ASME/ASCE/AHS/ASC Structures, Structural Dynamics and Materials Conference. https://doi.org/10.2514/6.2005-1811

25. Sanford G, Biskner A, Murphey T (2010) Large strain behavior of thin unidirectional composite flexures. In: 51st AIAA/ASME/ASCE/AHS/ASC Structures, Structural Dynamics, and Materials Conference. https://doi.org/10.2514/6.2010-2698

26. Duncan JL, Ding SC, Jiang WL (1999) Moment-curvature measurement in thin sheet–part I: equipment. Int J Mech Sci. 41(3):249–260. https://doi.org/10.1016/S0020-7403(98)00031-9

27. Ben Zineb T, Sedrakian A, Billoet JL (2003) An original pure bending device with large displacements and rotations for static and fatigue tests of composite structures. Compos B Eng. 34(5):447–458. https://doi.org/10.1016/S1359-8368(03)00017-9

28. Murphey TW, Peterson ME, Grigoriev MM (2015) Large Strain Four-Point Bending of Thin Unidirectional Composites. J Spacecr Rockets. 52(3):882–895. https://doi.org/10.2514/1.A32841

29. Antherieu G, Connesson N, Favier D, Mozer P, Payan Y (2016) Principle and Experimental Validation of a new Apparatus Allowing Large Deformation in Pure Bending: Application to thin Wire. Exp Mech. 56(3):475–482. https://doi.org/10.1007/s11340-015-0102-5

30. Fernandez JM, Murphey TW (2018) A simple test method for large deformation bending of thin high strain composite flexures. In: 2018 AIAA Spacecraft Structures Conference. https://doi.org/10.2514/6.2018-0942

31. Sharma AH, Rose TJ, Seamone A, Murphey TW, López Jiménez F (2019) Analysis of the column bending test for large curvature bending of high strain composites. In: AIAA Scitech 2019 Forum. https://doi.org/10.2514/6.2019-1746

32. Fernandez JM, Rose GK et al. (2018) An advanced composites-based solar sail system for interplanetary small satellite missions. In: 2018 AIAA Spacecraft Structures Conference. https://doi.org/10.2514/6.2018-1437

33. Lee AJ, Fernandez JM (2018) Mechanics of bistable two-shelled composite booms. In: 2018 AIAA Spacecraft Structures Conference. https://doi.org/10.2514/6.2018-0938

34. Rose TJ, Medina K, Francis W, Kwok K, Bergan A, Fernandez JM (2019) Viscoelastic behaviors of thin-ply high strain composites. In: AIAA Scitech 2019 Forum. https://doi.org/10.2514/6.2019-2027

35. Firth JA, Pankow MR (2020) Minimal Unpowered Strain-Energy Deployment Mechanism for Rollable Spacecraft Booms: Ground Test. J Spacecr Rockets. 57(2):346–353. https://doi.org/10.2514/1.A34565

36. Zehnder AT, Patel V, Rose TJ (2020) Micro-CT Imaging of Fibers in Composite Laminates under High Strain Bending. Exp Tech. 44(5):531–540. https://doi.org/10.1007/s40799-020-00374-9

37. Rose TJ, Calish J, López Jiménez F (2020) Modeling of viscoelasticity in thin flexible composites using coincident element method. In: AIAA Scitech 2020 Forum. https://doi.org/10.2514/6.2020-0693

38. Long Y, Rique O, Fernandez JM, Bergan A, Salazar JE, Yu W (2022) Simulation of the column bending test using an anisotropic viscoelastic shell model. Compos Struct. 288:115376. https://doi.org/10.1016/j.compstruct.2022.115376

39. Yapa Hamillage M, Leung C, Kwok K (2022) Viscoelastic modeling and characterization of thin-ply composite laminates. Compos Struct. 280:114901. https://doi.org/10.1016/j.compstruct.2021.114901

40. Aller B, Pellegrino S, Kinkaid N, Mejia-Ariza J, Otis R, Chan P et al (2023) Strain measurement in coilable thin composite shells with embedded fiber bragg grating sensors. In: AIAA Scitech 2023 Forum. https://doi.org/10.2514/6.2023-2399

41. DIN EN ISO 527-2 (2012) Plastics – Determination of tensile properties – Part 2: Test conditions for moulding and extrusion plastics (ISO 527-2:2012); German version EN ISO 527-2:2012

42. Turek DE (1993) On the tensile testing of high modulus polymers and the compliance correction. Polym Eng Sci. 33(6):328–333. https://doi.org/10.1002/pen.760330604

43. Jia N, Kagan VA (2000) Interpretations of tensile properties of polyamide 6 and PET based thermoplastics using ASTM and ISO procedures. In: Peraro JS (ed) Limitations of test methods for plastics. ASTM International, West Conshohocken, Pennsylvania, pp 54–71. https://doi.org/10.1520/STP14342S

44. DIN EN ISO 527-1 (2019) Plastics – Determination of tensile properties – Part 1: General principles (ISO 527-1:2019); German version EN ISO 527-1:2019

45. DIN EN 2002-001 (2006) Aerospace series – Metallic materials – Test methods – Part 1: Tensile testing at ambient temperature; German and English version EN 2002-001:2005

46. Cottrell AH (1953) LXXXVI. A note on the Portevin-Le Chatelier effect. Philos Mag Ser 7 44(355):829–832. https://doi.org/10.1080/14786440808520347

47. Klusemann B, Fischer G, Böhlke T, Svendsen B (2015) Thermomechanical characterization of Portevin-Le Châtelier bands in AlMg3 (AA5754) and modeling based on a modified Estrin-McCormick approach. Int J Plast. 67:192–216. https://doi.org/10.1016/j.ijplas.2014.10.011

48. Yilmaz A (2011) The Portevin-Le Chatelier effect: a review of experimental findings. Sci Technol Adv Mater. 12(6):063001. https://doi.org/10.1088/1468-6996/12/6/063001

49. Gao J, Chen W, Chen J, Hu J, Zhao B, Zhang D et al (2022) Accuracy Analysis on Counterweight-Balanced Column Bending Test. Exp Mech. 62(1):137–150. https://doi.org/10.1007/s11340-021-00767-w

50. Sharma AH, Perez R, Bearns NW, Rose TJ, López Jiménez F (2021) Some considerations involving testing guidelines for large curvature bending of high strain composites using the column bending test. In: AIAA Scitech 2021 Forum. https://doi.org/10.2514/6.2021-0196

51. Ubamanyu K, Pellegrino S (2023) Nonlinear behavior of IM7 carbon fibers in compression leads to bending nonlinearity of high-strain composites. In: AIAA Scitech 2023 Forum. https://doi.org/10.2514/6.2023-0580

52. Paros JM, Weisbord L (1965) How to design flexure hinges. Mach Des. 37:151–156

53. Lobontiu N, Paine JSN, Garcia E, Goldfarb M (2001) Corner-Filleted Flexure Hinges. J Mech Des. 123(3):346–352. https://doi.org/10.1115/1.1372190

54. ASTM D6272 (2010) Standard test method for flexural properties of unreinforced and reinforced plastics and electrical insulating materials by four-point bending

55. Mujika F, Arrese A, Adarraga I, Oses U (2016) New correction terms concerning three-point and four-point bending tests. Polymer Test. 55:25–37. https://doi.org/10.1016/j.polymertesting.2016.07.025

56. Ritter JE, Wilson WRD (1975) Frictional Effects in Four-Point Bending. ASLE Trans. 18(2):130–134. https://doi.org/10.1080/05698197508982755

57. Wisnom MR (1990) Limitations of linear elastic bending theory applied to four point bending of unidirectional carbon fibre-epoxy. In: 31st Structures, Structural Dynamics and Materials Conference. Reston, Virginia: American Institute of Aeronautics and Astronautics pp 740–747. https://doi.org/10.2514/6.1990-960

58. Tolf G, Clarin P (1984) Comparison between flexural and tensile modulus of fibre composites. Fibre Sci Technol. 21(4):319–326. https://doi.org/10.1016/0015-0568(84)90035-6

59. Meyer P, Traub H, Hühne C (2022) Actuated adaptive wingtips on transport aircraft: Requirements and preliminary design using pressure-actuated cellular structures. Aerosp Sci Technol. 128:107735. https://doi.org/10.1016/j.ast.2022.107735

60. Meyer P, Hühne C, Bramsiepe K, Krueger W (2023) Aeroelastic analysis of actuated adaptive wingtips based on Pressure-actuated cellular structures. In: AIAA Scitech 2023 Forum. https://doi.org/10.2514/6.2023-0825

61. Meyer P, Lück S, Spuhler T, Bode C, Hühne C, Friedrichs J et al (2021) Transient Dynamic System Behavior of Pressure Actuated Cellular Structures in a Morphing Wing. Aerospace. 8(3):89. https://doi.org/10.3390/aerospace8030089